Super-resolution chromatin tracing reveals domains and cooperative interactions in single cells

Bogdan Bintu[1,6], **Leslie J. Mateo**[2,6], **Jun-Han Su**[1], **Nicholas A. Sinnott-Armstrong**[3], **Mirae Parker**[4,5], **Seon Kinrot**[1], **Kei Yamaya**[2], **Alistair N. Boettiger**[2,7,*], and **Xiaowei Zhuang**[1,7,*]

[1]Howard Hughes Medical Institute, Department of Chemistry and Chemical Biology, Department of Physics, Harvard University, Cambridge, MA 02138

[2]Department of Developmental Biology, Stanford University, Stanford, CA 94305

[3]Department of Genetics, Stanford University, Stanford, CA 94305

[4]Department of Physics, Stanford University, Stanford, CA 94305

[5]Current address: Department of Computational Systems Biology, Massachusetts Institute of Technology. Cambridge, MA 02139

[6]These authors contributed equally to this work

[7]These authors contributed equally to this work

Abstract

The spatial organization of chromatin is pivotal for regulating genome functions. We report an imaging method for tracing chromatin organization with kilobase- and nanometer-scale resolution, unveiling chromatin conformation across topologically associating domains (TADs) in thousands of individual cells. Our imaging data revealed TAD-like structures with globular conformation and sharp domain boundaries in single cells. The boundaries varied from cell to cell, occurring with non-zero probabilities at all genomic positions, but preferentially at CCCTC-binding factor (CTCF)- and cohesin-binding sites. Notably, cohesin depletion, which abolished TADs at the population-average level, did not diminish domain structures in single cells, but eliminated preferential TAD-like boundary positions. Moreover, we observed wide-spread, cooperative, multi-way chromatin interactions, which remained after cohesin depletion. These results provide critical insight into the mechanisms underlying chromatin domain and hub formation.

Three-dimensional (3D) organization of the genome and cis interactions between genomic loci regulate many cellular processes, including gene expression, DNA replication, and DNA damage repair (1–6). Recent development of chromosome conformation capture

technologies, such as Hi-C (7), have greatly enriched our understanding of chromatin organization (4–6), revealing genome-wide structural features, such as topologically associating domains (TADs) and CTCF-dependent chromatin loops (8–12).

TADs are revealed in ensemble-averaged Hi-C contact maps as domains within which chromatin shows high contact probability (8–11). TADs tend to coincide with epigenetic domains, harbor co-regulated genes, and are generally conserved across cell types and species (4–6, 8–11). At a finer scale, TADs are divided into smaller domains with enhanced contact frequency, named sub-TADs (or contact domains), which are more variable across different cell types and thought to be involved in differential gene expression (6, 12, 13). Despite the proposed central role of these domain structures in chromatin organization and genome function, many of their basic properties remain unclear. In one view, it has been proposed that TADs represent a fundamental physical unit of the genome organization within individual cells, which promote intra-domain chromatin interactions but inhibit inter-domain interactions through spatial segregation (6, 14, 15). Recent super-resolution imaging studies provide partial support for this view by showing repressed chromatin domains as spatially segregated compact structures or nanocompartments in single cells (16, 17). However, recently reported single-cell Hi-C maps exhibit only a low density of chromatin contacts in individual cells and cell-to-cell variability in these contacts, leading to the debate of whether TADs exist in single cells (18–21). Although enrichment of chromatin contacts and, occasionally, large TAD-like structures could be observed in some genomic regions in single-cell Hi-C maps, the sparsity of contacts in these maps makes de novo identification of individual chromatin domains and domain boundaries challenging in single cells. An alternative view has thus been proposed that the genome is not packaged into spatially segregated domain structures in single cells, but is largely organized by recurrent pairwise interactions in an otherwise diverse ensemble of conformational configurations, with TADs being considered an emergent property from cell population averaging due to a tendency for contact enrichment within specific genomic regions in individual cells (19, 22). These two distinct models of TADs have different implications for our understanding of cis regulation of chromatin, but unfortunately a clear physical understanding of the TAD structure is still missing. Hi-C experiments have also identified "loop interactions", primarily observed at the boundaries of TADs or contact domains that harbor convergent CCCTC-binding factor (CTCF) sites (4–6, 12). Loop interactions have been proposed to facilitate interactions between regulatory sequences near the CTCF sites, such as enhancers and promoters, to induce gene activation (4, 12). While numerous pair-wise loop interactions have been observed in various genomes by Hi-C and other methods, higher-order interactions that involve more than two genomic loci are only beginning to be explored (23–27).

A major challenge in addressing the questions regarding chromatin organization is the lack of tools to provide a high-resolution visualization of the physical structure of chromatin in individual cells at the kilobase-to-megabase scale, which spans the sizes of genes and regulatory domains. Despite recent innovations in imaging methods that advance our knowledge of chromatin organization at this scale (see for example (16, 17, 28–31)), current microscopy approaches provide limited sequence information and resolution, and hence the power of high-spatial-resolution visualization is not accompanied by an ability to map the genomic sequences of chromatin structures de novo.

Multiplexed super-resolution FISH imaging for chromatin tracing

In this work, we developed a highly multiplexed super-resolution imaging approach for chromatin conformation tracing, which allows unbiased determination of both the structural features and their genomic coordinates with high resolution in single cells. To trace chromatin organization within and across TADs and sub-TAD, we imaged multiple 1.2–2.5 Mb regions of human chromosome 21 (Chr 21), traversing different numbers of TADs/sub-TADs, in multiple cell types. We partitioned each region of interest into consecutive 30-kb segments, and labeled and imaged individual segments following a sequential hybridization protocol, modified from our previous multiplexed RNA imaging method (32) and our previous lower (megabase) resolution chromatin imaging work (33). In the first step, we labeled the entire region with a library of ~12,000 – 25,000 primary Oligopaint probes (34, 35), each primary probe containing a 20-nt readout sequence that was unique for each 30-kb segment to facilitate multiplexed FISH imaging (Fig. 1A; Table S1) (33). Next, we added dye-labeled readout probes complementary to the readout sequences to allow 3D stochastic optical reconstruction microscopy (STORM) (36, 37) or 3D diffraction-limited imaging of individual 30-kb segments (Fig. 1A; Table S2). After each round, imaging one or two segments with single- or two-color imaging, the signal of the readout probes was extinguished by using a strand displacement reaction to remove the readout probes or by using photobleaching, or both, and the sequential process of readout-probe labeling and imaging was repeated until all segments were imaged (Fig. 1A). This allowed us to generate, for each cell, a 3D super-resolution image of the chromatin region of interest in numerous pseudocolors, each reporting the position and structure of a contiguous 30-kb segment (Fig. 1B), with <50 nm error in their localization and <5% error in their physical sizes (fig. S1).

These super-resolution chromatin images allowed us to measure the pairwise interactions between chromatin segments and compare with ensemble Hi-C measurements. We first focused on a 1.2-Mb region of Chr 21 (Chr21:28Mb-29.2Mb) in IMR90 fibroblast cells using STORM imaging. Quantitatively, we determined two complementary metrics between each pair of segments from the STORM images: the spatial overlap and the centroid-to-centroid distance (Fig. 1C). For each metric, we constructed a matrix for the entire imaged region for every copy of the chromosome imaged, and averaged across ~250 imaged chromosomes to obtain a population view, which can be compared to Hi-C (Fig. 1D-F). These matrices derived from imaging (Fig. 1E, F; fig. S2A) displayed similar domain structures (block-like structures) to those observed in the ensemble Hi-C contact-frequency matrix of the same genomic region (Fig. 1D). Both the spatial overlap and the spatial distance displayed high correlations with the Hi-C contact frequency, with Pearson correlation coefficients of 0.92 and −0.92, respectively (Fig. 1G, H). Interestingly, at the kb-to-Mb scale investigated here, the Hi-C contact frequency showed a power-law scaling with the spatial distance, with a scaling exponent of −4.9, similar to our previous observation at the Mb-to-whole chromosome scale (33), suggesting that this scaling is potentially a universal property.

We also performed diffraction-limited 3D imaging of each chromatin segment in the same multiplex fashion. The ensemble spatial-distance matrix derived from diffraction-limited imaging also showed similar domain structures (Fig. 1I; fig. S2B) and high correlation with

the ensemble Hi-C contact-frequency matrix (Fig. 1J). The multiplexed STORM and diffraction-limited imaging methods have complementary capabilities: the former provided high resolution information not accessible to the latter, such as the sizes and shapes of individual chromatin segments, whereas the latter allowed for faster image acquisition and higher throughput for the number of chromatin segments or cells imaged. Because the otherwise unresolvable chromatin segments can be separated and localized with high precision by sequential imaging, even the latter approach provided a super-resolution view of chromatin conformation, albeit not as high resolution as the STORM images. We used both approaches to interrogate chromatin organization at the single-cell level below.

Super-resolution chromatin tracing reveals TAD-like structures in single cells

Notably, our STORM images and spatial-overlap matrices of individual chromosomes in single cells often showed clear domain structures with higher intra-domain chromatin contact (overlap) frequency (Fig. 2A, B). We refer to these domains as TAD-like structures because of their similar appearance to TADs and sub-TADs in the ensemble-averaged contact matrices, although the boundaries of these single-cell domains varied from cell to cell. For instance, in the STORM images of two example cells, chromatin regions that belong to different ensemble sub-TADs showed extensive overlap in one cell but clear segregation in another cell (Fig. 2A, B). We identified and quantified the boundary positions of these TAD-like domains from the single-cell spatial-overlap matrices in an automated manner. The domain boundaries showed substantial cell-to-cell variation, and a non-zero probability to reside at any of the genomic positions throughout the imaged region (Fig. 2C). Moreover, the domain boundaries exhibited a preference to reside at genomic positions containing strong binding peaks of CTCF and cohesin (marked by one of its core subunits RAD21), as detected by chromatin immunoprecipitation sequencing (ChIP-seq) (38) (Fig. 2C, D), giving rise to the tendency for ensemble TAD and sub-TAD boundaries to align with these sites (4–6, 12). Remarkably, these domains often appeared as spatially segregated globular structures in the STORM images (Fig. 2B, fig. S3A,B). We quantified the spatial segregation using a separation score at each genomic position describing the level of spatial separation between chromatin on either side of the position (fig. S3A,B). The separation scores displayed nearly complete segregation at many of the identified single-cell domain boundaries (fig. S3; Fig. 2C).

Next, we took advantage of the higher throughput of diffraction-limited multiplexed imaging to investigate an extended 2-Mb genomic region (Chr21:28Mb-30Mb) in thousands of individual cells from three distinct cell lines: IMR90 lung fibroblasts, K562 erythroleukemia, and A549 lung epithelial carcinoma cells. Previous ensemble Hi-C data for IMR90 and K562 showed that this genomic region contains two TADs with cell-type specific sub-TADs (fig. S4A) (12). The ensemble spatial-distance and contact matrices derived from our imaging data again agree remarkably well with the ensemble Hi-C contact matrices for IMR90 and K562, and additionally allowed TAD and sub-TAD identifications in A549 cells (Fig. 3A-C; fig. S4). At the single-cell level, we observed TAD-like structures with globular 3D conformation and sharp domain boundaries in the images and spatial-

distance matrices of individual chromosomes in all three cell types (Fig. 3D-F). The domain boundary positions again showed cell-to-cell heterogeneity, with a non-zero probability to locate at any genomic positions within the 2-Mb imaged region, and showed a preference to reside at positions bound by CTCF and cohesin (Fig. 3G-I, fig. S5).

To test whether these cell-to-cell variations in domain boundaries were caused by different cell-cycle states, we used immuno-labeling of the cell-cycle regulator, geminin, along with the DAPI stain to separate the cells into G1, S and G2 phases approximately (fig. S6A, B). The ensemble spatial-distance matrices were similar among all three phases, without any notable change in the TAD/sub-TAD boundaries (fig. S6C), consistent with previous results (21, 39). We observed moderate changes in TAD strength, characterized by the TAD insulation score, suggesting a moderate weakening of ensemble TADs from G1 to G2 (fig. S6D)), also in agreement with previous results (21). Notably, single-cell TAD-like structures were observed in all three phases (fig. S6E), and the cell-to-cell variability and preferential positioning of domain boundaries were all similar among the three phases (fig. S6F, G), suggesting that the observed cell-to-cell variations in domain boundary positions were not primarily due to differences in cell-cycle state.

Next, we imaged an additional 2-MB region (Chr21:18.6Mb-20.6Mb) that contained no discernable TAD boundaries in the ensemble Hi-C contact matrix (fig. S7A) (12). Similarly, our ensemble spatial-distance matrix derived from imaging also did not show any discernable domains (fig. S7B). However, the single-cell spatial-distance matrices often showed clearly visible TAD-like structures with sharp domain boundaries (fig. S7C), and the average domain boundary strength was similar to that observed for the ensemble-TAD/sub-TAD-containing 2-Mb region (Chr21:28Mb-30Mb) described above (fig. S7D). In contrast to the Chr21:28Mb-30Mb region, the Chr21:18.6–20.6Mb region showed largely uniform probability for the presence of single-cell domain boundaries throughout the region (fig. S7E), explaining the lack of domain boundaries in the ensemble matrix of this region.

TAD-like structures remain in single cells after cohesin depletion

We next investigated how chromatin structures change upon removal of the architectural protein, cohesin. DNA-extrusion by cohesin complexes has been proposed as a mechanism responsible for ensemble TAD formation (22, 40). Previous studies have shown that the depletion of cohesin causes elimination of TADs at the ensemble level, whereas the A/B compartment structures enriched for active and inactive chromatin are retained (25, 41).

Using HCT116 cells with an auxin-inducible degron fused to a core cohesin subunit RAD21 (42), we compared the chromatin structures under both induced and uninduced conditions (Fig. 4; figs. S8–S10). We imaged a 2.5-MB region (Chr21:34.6Mb-37.1Mb) that shows several pronounced TAD structures within a single type A compartment (fig. S8A, top panel), in addition to the genomic region described earlier (Chr21:28Mb-30Mb), which shows less pronounced TAD boundaries super-imposed on A/B compartment structures in ensemble Hi-C matrices of HCT116 cells (fig. S9A-C, top panels) (25) . The ensemble spatial-distance matrices derived from our imaging data were similar to the ensemble Hi-C matrices for both regions (Fig. 4A, left panel; fig. S8B, top panel; fig. S9D-F, top panels). As

expected, upon 6h of auxin treatment to induce cohesin degradation, the population-averaged TADs and sub-TADs within the imaged regions were largely eliminated whereas the A/B compartment structures retained (Fig. 4A, right panel; fig. S8B, bottom panel; fig. S9D-F, bottom panels), consistent with Hi-C results (fig. S8A, bottom panel; fig. S9A-C, bottom panels) (25). Notably, the chromatin domains observed in single cells persisted after cohesin degradation (Fig. 4B; fig. S10A). Moreover, the domain boundary strengths remained similar between cells with and without cohesin (Fig. 4C; fig. S10B), and the average number of boundaries within the regions also remained similar between cells with and without cohesin, as reflected by the similar values for the mean probability for identifying a domain boundary averaged over all genomic positions (Fig. 4D; fig. S10C). What was notably different in the absence of a functional cohesin complex was that the positions of these domain boundaries became largely uniformly distributed along the genomic coordinate, and no longer exhibited preferential positioning at CTCF/cohesin sites as observed in the presence of cohesin (Fig. 4D; fig. S10C). These results indicate that cohesin is not required for the maintenance of TAD-like structures in single cells, and that the role of cohesin in the formation of ensemble TADs is to establish preferred genomic boundaries for the single-cell domains. On the other hand, preferential boundary positions for A/B compartment were still observed in individual cohesin-deplete cells, similar to those observed for untreated cells (fig. S10D), consistent with the observation that A/B compartments at the ensemble level were retained after cohesin depletion.

Interestingly, we noticed that cohesin depletion strongly hindered but did not completely stop cell division in HCT116 cells (fig. S11A, B), which allowed us to examine chromatin structures in cells that had gone through a cell cycle without cohesin. We added the modified base 5-ethynyl-2′-deoxyuridine (EdU) to cells for an additional 12h in the presence of auxin after 6h of initial auxin treatment, and used the EdU and geminin signals to select cells that likely had passed through mitosis and re-entered G1 phase (EdU+/geminin- cells) (fig. S11C-F). We observed that, despite the removal of ensemble TAD boundaries (fig. S11G), single-cell TAD-like domain structures also remained in this population of EdU+/geminin- cells (fig. S11H-J). Because cells undergo major chromatin reorganization during mitosis (39), these TAD-like structures were likely re-stablished after mitosis. These data thus suggest that cohesin may not be required for the establishment of domain separation in single cells either, though future experiments are needed to further test this notion.

Cooperative, higher-order chromatin interactions are wide spread in single cells

In addition, our chromatin tracing approach allowed us to study higher-order interactions between three or more chromatin loci. We first examined if the interaction between two CTCF sites facilitates or inhibits the interaction with a third. Such higher-order interactions showed cell-to-cell variation, as illustrated in the STORM images (Fig. 5A). Interestingly, when two CTCF sites (represented by letters "A" and "B") showed overlap, we frequently noticed an enhanced overlap of both sites with a third CTCF site, represented by the letter "C", as exemplified by the triplet of CTCF sites (A1, B1 and C1) in Fig. 5B. Since we consider only ordered A, B, and C sites such that C was not between A and B on the

genomic coordinate, this facilitation effect cannot be trivially explained by the polymeric nature of chromatin. We systematically quantified this type of facilitated chromatin interactions for all ~500 combinations of such ordered triplets of CTCF sites in the STORM-imaged region of IMR90 cells. Among all triplets analyzed, ~80% showed such facilitated interactions (Fig. 5C).

We next asked whether this cooperative interaction is specific to CTCF sites or is generic to other chromatin loci. We analyzed such three-site interactions for all segments in our imaged regions in all cell types studied (IMR90, K562, A549 and HCT116). We observed that, despite notable quantitative differences observed across different genomic regions and different cell types, contact between two chromatin segments in general tended to increase the probability for these segments to contact a third segment, even when the segments did not harbor CTCF sites (Fig. 5D-F). Moreover, upon auxin-induced cohesin depletion, this facilitated high-order interaction persisted (Fig. 5E, F).

Discussion

Our multiplexed, super-resolution imaging method allows the 3D organization of chromatin to be traced with nanometer- and kilobase-scale resolution in thousands of single cells. These imaging data directly revealed diverse chromatin configurations in individual cells, providing insights into the nature of chromatin folding. We observed that chromatin in single cells forms TAD-like domain structures with sharp domain boundaries, and these domain structures often adopt globular conformation with strong physical segregation between neighboring domains. The direct visualization of chromatin conformation, high-detection efficiency of individual genomic loci, and high density single-cell interaction or distance maps offered by our imaging approach allowed us to identify these single-cell domain structures that are challenging to detect by previous methods. Hence, our data demonstrates that TAD-like domains are physical structures present in single cells and not an emergent property of population averaging. However, the boundaries positions of these single-cell domains show substantial cell-to-cell variation, therefore the ensemble TAD boundaries are emergent properties of population averaging due to the preferential positioning of single-cell domain boundaries at sites occupied by CTCF/cohesin. The observed cell-to-cell variability may reflect the dynamic nature of the single-cell domains but is not primarily caused by different cell-cycle states. It is also possible that the epigenetic modification profiles vary from cell to cell, contributing to these observed variations in domain boundary positions. Strikingly, these single-cell domain structures persist even after depletion of cohesin, a treatment that eliminates TADs and sub-TADs at the population-average level. The loop extrusion model (22, 40), in which cohesin complexes extrude DNA until stopped by a pair of CTCF motifs, has been proposed to explain the formation of TADs and sub-TADs at the population-average level (22, 25, 40, 41). However, in its simplest form, loop extrusion does not lead to strong physical segregation of chromatin domains in single cells (22). Our data indicate that cohesin is not required for the maintenance of the observed single-cell TAD-like domain structures, and is likely not required for the initial establishment of these structures either. However, the preferential positioning of the single-cell domain boundaries at CTCF sites was abolished after cohesin depletion, suggesting its dependence on cohesin-

CTCF interaction, possibly through loop extrusion, thereby explaining the loss of ensemble TADs upon cohesin depletion.

In addition, we observed higher-order interactions between multiple chromatin loci and many three-way contacts were observed at higher frequencies than expected from the observed frequency of pairwise interactions, indicative of a form of cooperativity. Such cooperative multi-way interaction appears to be a general property of chromatin not limited to specific regulatory elements. It has been suggested that the collision between two loop extruders could facilitate three-way chromatin interactions (26, 43, 44). Our observation that the cooperative three-way interactions occur even after cohesin depletion indicate that these observed higher-order interactions can arise from a mechanism distinct from the cohesin-based loop extrusion, though our observations do not exclude the possibility that the loop extrusion model could function in parallel to induce higher-order chromatin interactions.

Together, our observations of chromatin organization in single cells expand upon the emerging view that genome packaging is more complex than pairwise interactions (45). Our imaging method, which provides a high-resolution physical view of chromatin conformation of targeted genomic regions, can complement sequencing-based genome-wide methods for investigating chromatin organization beyond pairwise interactions. The combination of these methods will help us better understand the complex structural landscape of the genome, tackling problems ranging from interactions among multiple cis-regulatory elements to overall folding conformation of the chromosomes.

Methods Summary

Each genomic region of interest was divided into 30 kb segments, and target oligonucleotides for these segments were designed computationally. Target oligonucleotides for each segment were concatenated to a unique readout sequence, along with primer regions for selection and amplification, to constitute the primary probe. The primary probes were synthesized through array-based oligo-pool technology and amplified using PCR, and in vitro transcription followed by reverse transcription (32). These probes were hybridized to cells adhered to glass coverslips. The samples were mounted in a flow chamber connected to a custom fluidics system for iterative readout probe hybridization and imaged using a custom-assembled microscope (32, 33). Fluorescently labeled oligonucleotides complementary to the readout sequences of each segment, i.e. readout probes, were added by the fluidics system, hybridized for 10–30 minutes, and then rinsed out with a wash buffer. The labeled cells were then imaged by STORM and/or diffraction-limited microscopy. After imaging, the signal of the readout probes was extinguished either by stripping off the probes using DNA strand-displacement or by photobleaching the fluorescence, or both, and readout probes complementary to the next readout sequence(s) (associated with the next chromatin segment(s)) were added. The process was repeated until all chromatin segments were imaged, such that the multiplexed image of the whole genomic region of can be constructed with high resolution. Detailed probe design, synthesis and imaging methods, as well as methods for image analysis, for constructing spatial overlap, distance and contact matrices, and for single-cell domain analyses are described in the Materials and Methods section of the Supplementary Materials.

Supplementary Material

Refer to Web version on PubMed Central for supplementary material.

References and notes:

1. Bickmore WA, The spatial organization of the human genome. Annu. Rev. Genomics Hum. Genet. 14, 67–84 (2013). [PubMed: 23875797]

2. Levine M, Cattoglio C, Tjian R, Looping back to leap forward: Transcription enters a new era. Cell. 157, 13–25 (2014). [PubMed: 24679523]

3. Dekker J, Misteli T, Long-Range Chromatin Interactions. Cold Spring Harb. Perspect. Biol. 7, a019356 (2015). [PubMed: 26430217]

4. Dekker J, Mirny L, The 3D Genome as Moderator of Chromosomal Communication. Cell. 164, 1110–1121 (2016). [PubMed: 26967279]

5. Krijger PHL, De Laat W, Regulation of disease-associated gene expression in the 3D genome. Nat. Rev. Mol. Cell Biol. 17, 771–782 (2016). [PubMed: 27826147]

6. Yu M, Ren B, The Three-Dimensional Organization of Mammalian Genomes. Annu. Rev. Cell Dev. Biol. 33, 265–289 (2017). [PubMed: 28783961]

7. Lieberman-Aiden E et al., Comprehensive mapping of long-range interactions reveals folding principles of the human genome. Science (80-.). 326, 289–293 (2009).

8. Dixon JR et al., Topological domains in mammalian genomes identified by analysis of chromatin interactions. Nature. 485, 376–380 (2012). [PubMed: 22495300]

9. Nora EP et al., Spatial partitioning of the regulatory landscape of the X-inactivation centre. Nature. 485, 381–385 (2012). [PubMed: 22495304]

10. Sexton T et al., Three-Dimensional Folding and Functional Organization Principles of the Drosophila Genome. Cell. 148, 458–472 (2012). [PubMed: 22265598]

11. Hou C, Li L, Qin ZS, Corces VG, Gene Density, Transcription, and Insulators Contribute to the Partition of the Drosophila Genome into Physical Domains. Mol. Cell. 48, 471–484 (2012). [PubMed: 23041285]

12. Rao SSP et al., A 3D Map of the Human Genome at Kilobase Resolution Reveals Principles of Chromatin Looping. Cell. 159, 1665–1680 (2014). [PubMed: 25497547]

13. Phillips-Cremins JE et al., Architectural protein subclasses shape 3D organization of genomes during lineage commitment. Cell. 153, 1281–1295 (2013). [PubMed: 23706625]

14. Gibcus JH, Dekker J, The Hierarchy of the 3D Genome. Mol. Cell. 49, 773–782 (2013). [PubMed: 23473598]

15. Sexton T, Cavalli G, The role of chromosome domains in shaping the functional genome. Cell. 160, 1049–1059 (2015). [PubMed: 25768903]

16. Boettiger AN et al., Super-resolution imaging reveals distinct chromatin folding for different epigenetic states. Nature. 529, 418–422 (2016). [PubMed: 26760202]

17. Szabo Q et al., TADs are 3D structural units of higher-order chromosome organization in Drosophila. Sci. Adv. 4, 1–14 (2018).

18. Nagano T et al., Single-cell Hi-C reveals cell-to-cell variability in chromosome structure. Nature. 502, 59–64 (2013). [PubMed: 24067610]

19. Flyamer IM et al., Single-nucleus Hi-C reveals unique chromatin reorganization at oocyte-to-zygote transition. Nature. 544, 110–114 (2017). [PubMed: 28355183]

20. Stevens TJ et al., 3D structures of individual mammalian genomes studied by single-cell Hi-C. Nature. 544, 59–64 (2017). [PubMed: 28289288]

21. Nagano T et al., Cell-cycle dynamics of chromosomal organization at single-cell resolution. Nature. 547, 61–67 (2017). [PubMed: 28682332]

22. Fudenberg G et al., Formation of Chromosomal Domains by Loop Extrusion. Cell Rep. 15, 2038–2049 (2016). [PubMed: 27210764]

23. Olivares-Chauvet P et al., Capturing pairwise and multi-way chromosomal conformations using chromosomal walks. Nature. 540, 296–300 (2016). [PubMed: 27919068]

24. Beagrie RA et al., Complex multi-enhancer contacts captured by genome architecture mapping. Nature. 543, 519–524 (2017). [PubMed: 28273065]

25. Rao SSP et al., Cohesin Loss Eliminates All Loop Domains. Cell. 171, 305–320.e24 (2017). [PubMed: 28985562]

26. Allahyar A et al., Enhancer hubs and loop collisions identified from single-allele topologies. Nat. Genet. 50, 1151–1160 (2018). [PubMed: 29988121]

27. Quinodoz SA et al., Higher-Order Inter-chromosomal Hubs Shape 3D Genome Organization in the Nucleus. Cell. 174, 744–757.e24 (2018). [PubMed: 29887377]

28. Chen B et al., Dynamic imaging of genomic loci in living human cells by an optimized CRISPR/Cas system. Cell. 155, 1479–1491 (2013). [PubMed: 24360272]

29. Ricci MA, Manzo C, García-Parajo MF, Lakadamyali M, Cosma MP, Chromatin fibers are formed by heterogeneous groups of nucleosomes in vivo. Cell. 160, 1145–1158 (2015). [PubMed: 25768910]

30. Deng W, Shi X, Tjian R, Lionnet T, Singer RH, CASFISH: CRISPR/Cas9-mediated in situ labeling of genomic loci in fixed cells. Proc. Natl. Acad. Sci. 112, 11870–11875 (2015). [PubMed: 26324940]

31. Ma H et al., Multiplexed labeling of genomic loci with dCas9 and engineered sgRNAs using CRISPRainbow. Nat. Biotechnol. 34, 528–530 (2016). [PubMed: 27088723]

32. Chen KH, Boettiger AN, Moffitt JR, Wang S, Zhuang X, Spatially resolved, highly multiplexed RNA profiling in single cells. Science (80-.). 348 aaa6090 (2015). 10.1126/science.aaa6090

33. Wang S et al., Spatial organization of chromatin domains and compartments in single chromosomes. Science (80-.). 353, 598–602 (2016).

34. Beliveau BJ et al., Versatile design and synthesis platform for visualizing genomes with Oligopaint FISH probes. Proc. Natl. Acad. Sci. 109, 21301–21306 (2012). [PubMed: 23236188]

35. Beliveau BJ et al., Single-molecule super-resolution imaging of chromosomes and in situ haplotype visualization using Oligopaint FISH probes. Nat. Commun. 6, 7147 (2015). [PubMed: 25962338]

36. Rust MJ, Bates M, Zhuang X, Sub-diffraction-limit imaging by stochastic optical reconstruction microscopy (STORM). Nat. Methods. 3, 793–795 (2006). [PubMed: 16896339]

37. Huang B, Wang W, Bates M, Zhuang X, Three-dimensional super-resolution imaging by stochastic optical reconstruction microscopy. Science (80-.). 319, 810–813 (2008).

38. The ENCODE Project. Consortium et al., An integrated encyclopedia of DNA elements in the human genome. Nature. 489, 57–74 (2012). [PubMed: 22955616]

39. Naumova N et al., Organization of the mitotic chromosome. Science. 342, 948–53 (2013). [PubMed: 24200812]

40. Sanborn AL et al., Chromatin extrusion explains key features of loop and domain formation in wild-type and engineered genomes. Proc. Natl. Acad. Sci. 112, E6456–E6465 (2015). [PubMed: 26499245]

41. Schwarzer W et al., Two independent modes of chromatin organization revealed by cohesin removal. Nature. 551, 51–56 (2017). [PubMed: 29094699]

42. Natsume T, Kiyomitsu T, Saga Y, Kanemaki MT, Rapid Protein Depletion in Human Cells by Auxin-Inducible Degron Tagging with Short Homology Donors. Cell Rep. 15, 210–218 (2016). [PubMed: 27052166]

43. Haarhuis JHI et al., The Cohesin Release Factor WAPL Restricts Chromatin Loop Extension. Cell. 169, 693–707.e14 (2017). [PubMed: 28475897]

44. Busslinger GA et al., Cohesin is positioned in mammalian genomes by transcription, CTCF and Wapl. Nature. 544, 503–507 (2017).

45. Hnisz D, Shrinivas K, Young RA, Chakraborty AK, Sharp PA, A Phase Separation Model for Transcriptional Control. Cell. 169, 13–23 (2017). [PubMed: 28340338]

46. Moffitt JR et al., High-throughput single-cell gene-expression profiling with multiplexed error-robust fluorescence in situ hybridization. Proc. Natl. Acad. Sci. 113, 11046–11051 (2016). [PubMed: 27625426]

47. Bao W, Kojima KK, Kohany O, Repbase Update, a database of repetitive elements in eukaryotic genomes. Mob. DNA. 6, 11 (2015). doi:10.1186/s13100-015-0041-9 [PubMed: 26045719]

48. Narita M et al., Rb-mediated heterochromatin formation and silencing of E2F target genes during cellular senescence. Cell. 113, 703–716 (2003). [PubMed: 12809602]

49. Solovei I et al., Spatial preservation of nuclear chromatin architecture during three-dimensional fluorescence in situ hybridization (3D-FISH). Exp. Cell Res. 276, 10–23 (2002). [PubMed: 11978004]

50. Branco MR, Pombo A, Intermingling of chromosome territories in interphase suggests role in translocations and transcription-dependent associations. PLoS Biol. 4, 780–788 (2006).

51. Markaki Y et al., The potential of 3D-FISH and super-resolution structured illumination microscopy for studies of 3D nuclear architecture: 3D structured illumination microscopy of defined chromosomal structures visualized by 3D (immuno)-FISH opens new perspectives for stud. BioEssays. 34, 412–426 (2012). [PubMed: 22508100]

52. Dempsey GT, A User's Guide to Localization-Based Super-Resolution Fluorescence Imaging (Elsevier Inc, ed. 4, 2013; 10.1016/B978-0-12-407761-4.00024-5), vol. 114.

53. Rasnik I, McKinney SA, Ha T, Nonblinking and long-lasting single-molecule fluorescence imaging. Nat. Methods. 3, 891–893 (2006). [PubMed: 17013382]

54. Matthiesen SH, Hansen CM, Fast and non-toxic in situ hybridization without blocking of repetitive sequences. PLoS One. 7, e40675 (2012). 10.1371/journal.pone.0040675 [PubMed: 22911704]

55. Machinek RRF, Ouldridge TE, Haley NEC, Bath J, Turberfield AJ, Programmable energy landscapes for kinetic control of DNA strand displacement. Nat. Commun. 5, 5324 (2014). doi: 10.1038/ncomms6324 [PubMed: 25382214]

56. Babcock H, Sigal YM, Zhuang X, A high-density 3D localization algorithm for stochastic optical reconstruction microscopy. Opt. Nanoscopy. 1, 6 (2012).
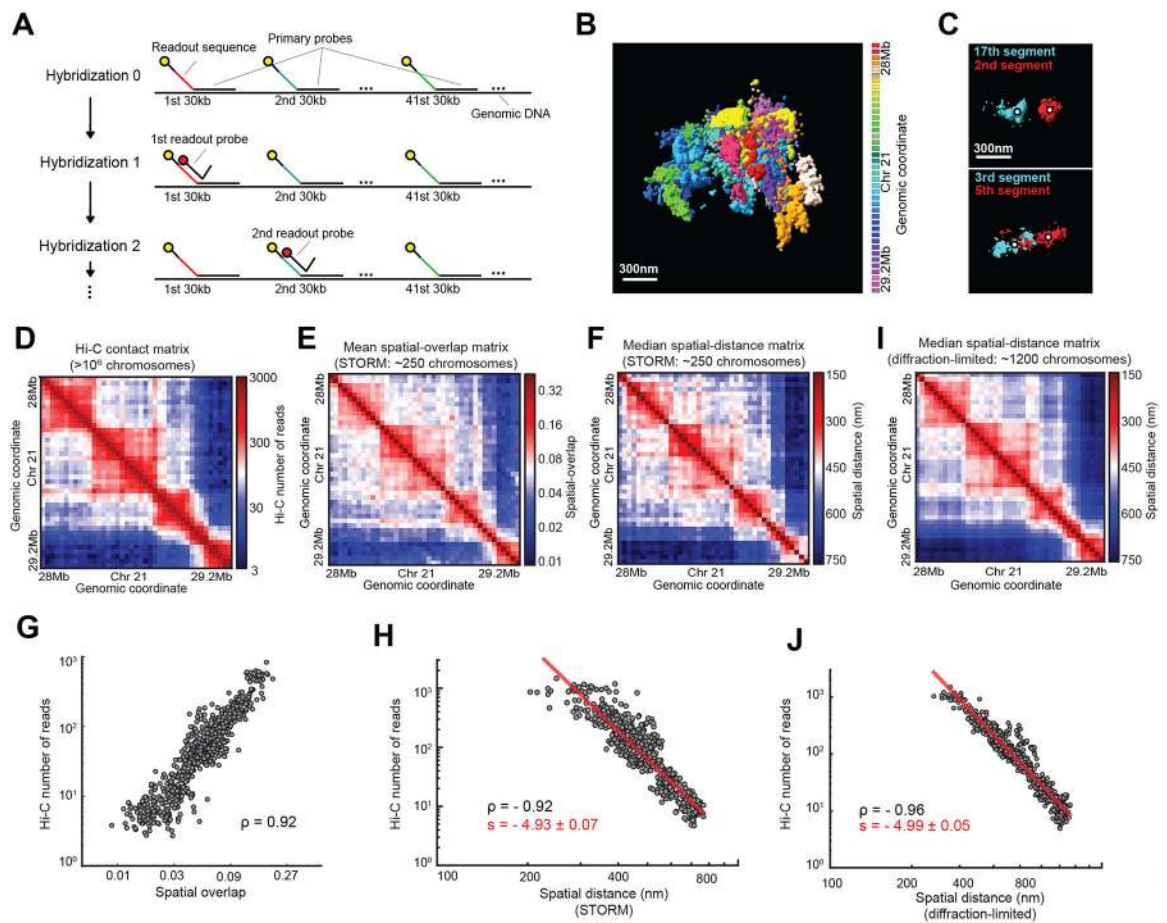
Fig. 1. Multiplex FISH imaging for high-resolution chromatin tracing allows de novo identification of TADs and sub-TADs.

(**A**) A scheme of the imaging approach. The genomic region of interest is partitioned into consecutive 30-kb segments and first hybridized with primary oligonucleotide probes that label all segments. These probes contained a readout sequence unique to each 30-kb segment. Each segment is labeled by ~300 probes but only one is shown. Readout probes complementary to the readout sequences are then added sequentially, allowing the imaging of individual 30-kb segments. (**B**) Composite 3D STORM images of 41 consecutive 30-kb chromatin segments in a 1.2-Mb region of Chromosome 21 (Chr21:28Mb-29.2Mb), in 41 pseudocolors, in one copy of Chr21 of an IMR90 cell. (**C**) 3D STORM images of two pairs of chromatin segments showing different degree of overlap, but similar distances between their center positions (marked by white dots). (**D**) Ensemble Hi-C contact frequency matrix for the 1.2-Mb genomic region binned at 30-kb resolution (data from (12)). (**E, F**) Mean spatial-overlap matrix (E) and median spatial-distance matrix (F) for the same region derived from multiplexed STORM imaging. Each element of the matrix corresponds to the mean value of the overlap fraction (E) and median value of the center-of-mass distance (F) between a pair of the chromatin segments across ~250 imaged chromosomes. (**G**) Correlation between the Hi-C contact frequency and the mean spatial overlap shown in (D) and (E), respectively. (**H**) Correlation between the Hi-C contact frequencies and median spatial distances shown in (D) and (F), respectively. (**I**) Median spatial-distance matrix for

the same genomic region derived from multiplexed diffraction-limited imaging of ~1200 chromosomes. (**J**) Correlation between the Hi-C contact frequencies and median spatial distances shown in (D) and (I), respectively. The Pearson correlation coefficients (ρ) are 0.92, −0.92 and −0.96 in (G), (H) and (J) respectively. The red lines in (H) and (J) are power-law fits with scaling exponents (s) equal to −4.93 ± 0.07 and −4.99 ± 0.05 in (H) and (J), respectively.
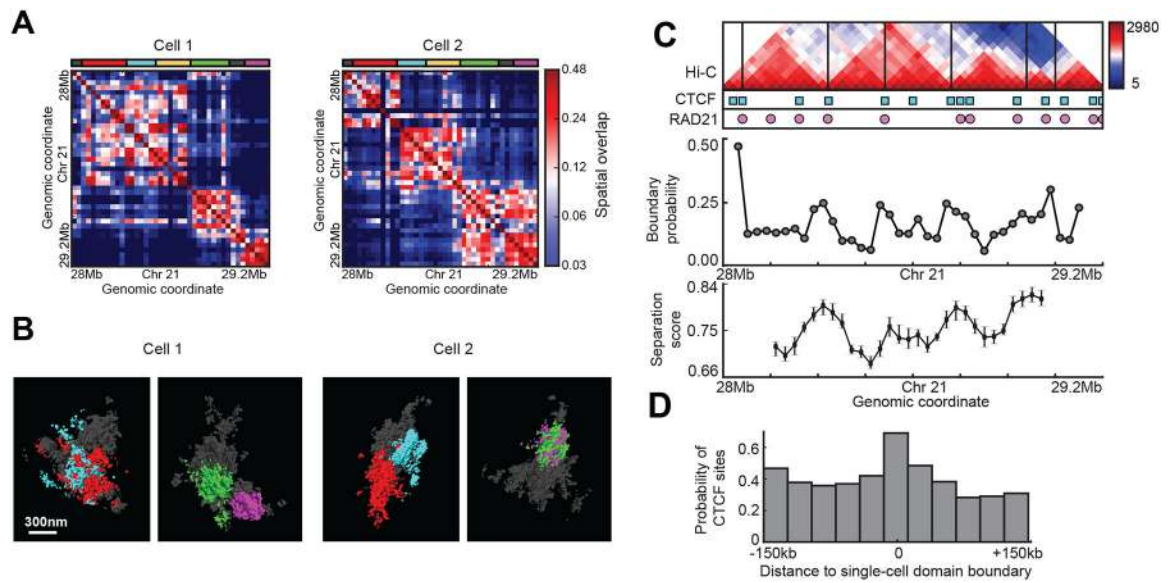
Fig. 2. Chromatin forms TAD-like domain structures with spatially segregated globular conformations in single cells.

(A) The spatial-overlap matrices of the 1.2-Mb genomic region (Chr21:28Mb-29.2Mb) imaged in one of the two copies of Chr21 from two individual IMR90 cells. The genomic regions marked in red, cyan, yellow, green, and purple correspond to the five sub-TADs observed at the population-average level. **(B)** Multiplexed 3D STORM images corresponding to the two chromosomes shown in (A). The chromatin segments comprising two pairs of ensemble sub-TADs marked as red and cyan or green and purple in (A) are pseudo-colored in the same color code. Only one pair of sub-TADs is highlighted in colors per image for the ease of visualization, and the other segments in the region of interest are displayed in gray. Each chromatin image is rotated independently to allow the best visualization of the color-highlighted chromatin regions. **(C)** Top: Ensemble Hi-C contact frequency map with sub-TAD boundaries indicated with black lines, shown together with the sites bound by CTCF (cyan squares) and cohesin (represented by RAD21, magenta circles), as determined by ChIP-seq in IMR90 cells (38). Middle: The probability (fraction of the ~250 imaged chromosomes) for each genomic location to appear as a single cell domain boundary. Bottom: The median separation score for each genomic location across the ~250 imaged chromosomes. Error bars indicate 95% confidence intervals derived by resampling (n ~ 250 chromosomes). The separation score is determined as shown in fig. S3. **(D)** The occurrence probability of CTCF/cohesin sites as a function of genomic distance from single-cell domain boundaries. Individual single-cell domain boundaries were aligned and the relative positions of CTCF ChIP peaks (that colocalize with RAD21 peaks) up to 150 kb on either side of the domain boundaries were histogrammed at 30kb resolution. The histograms were normalized by dividing by the total number of boundaries.
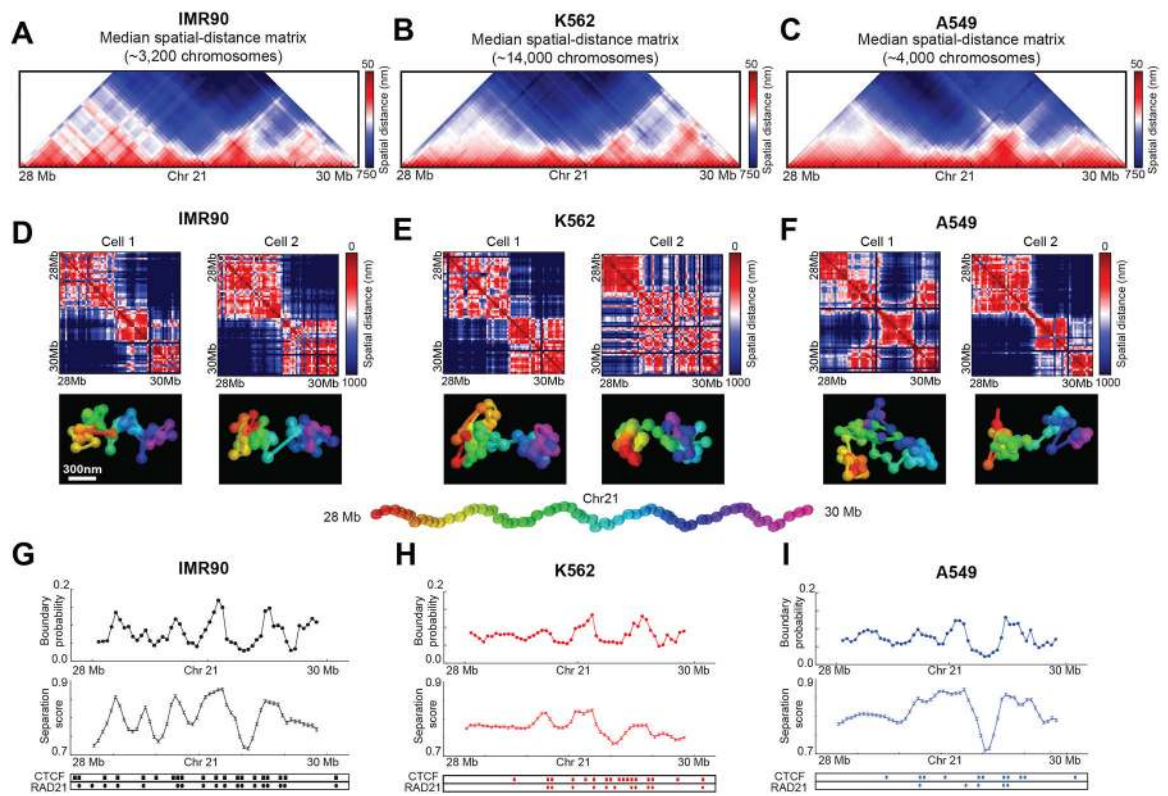
Fig. 3. Single-cell TAD-like structures are formed across cell types.
(**A-C**) Median spatial-distance matrices for the 2-Mb genomic region of interest (Chr21:28Mb-30Mb) in three cell types: IMR90 lung fibroblast (A), K562 erythroleukemia (B) and A549 carcinomic epithelial cells (C). The number of chromosomes imaged (~3,000–14,000) is indicated above each matrix. (**D-F**) Single-cell spatial-distance matrices of the imaged region (upper) and the corresponding pseudo-colored images showing 3D positions of the chromatin segments in each chromosome (lower). Two example cells (and one chromosome copy from each cell) are shown for each of the three cell types (D: IMR90; E: K562; F: A549). (**G-I**) Top: The probability for each genomic position to be a boundary of a single-cell domain for each of the three cell types (G: IMR90; H: K562; I: A549). Bottom: The mean separation score for each genomic coordinate for each cell type. Error bars indicate 95% confidence intervals (n ~3,200, 14,000, and 4,000 chromosomes for IMP90, K652 and A549 cells, respectively). The binding sites of CTCF and cohesin (marked by RAD21) determined by ChIP-seq for each cell type (38) are indicated with squares and circles respectively.
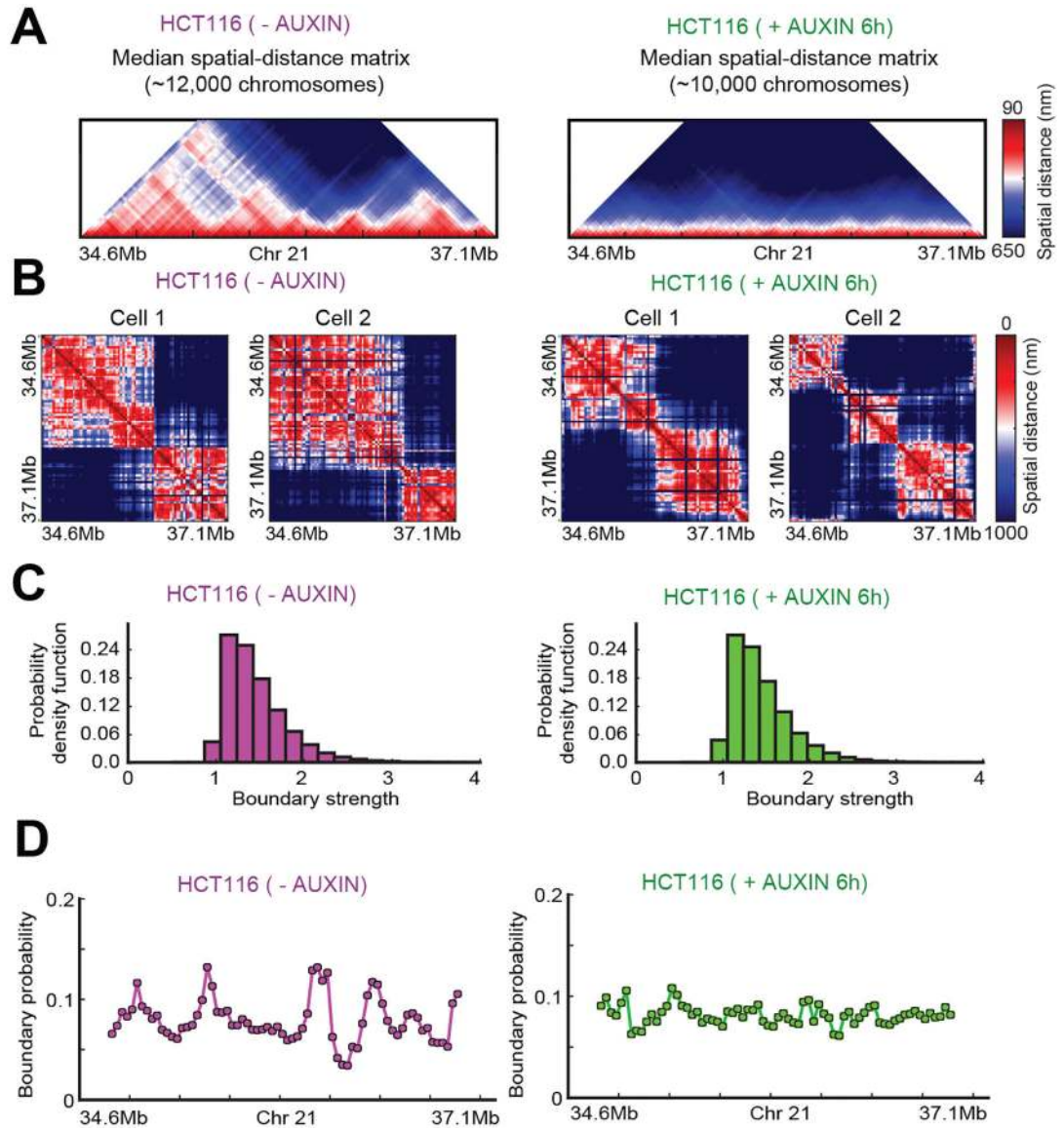
Fig. 4. Single-cell TAD-like structures are present in cells lacking a functional cohesin complex.
(A) Median spatial-distance matrices for the 2.5-Mb genomic region of interest (Chr21:34.6Mb-37.1Mb) in the transgenic HCT116 cell line without (left) or with (right) auxin treatment to induce cohesin degradation. **(B)** Example single-cell spatial-distance matrices without (left) and with (right) auxin treatment. **(C)** The distribution of boundary strengths in the imaged region for cells without (left) and with (right) auxin treatment. For each identified domain boundary on a single-cell spatial-distance matrix, the boundary strength describes how steeply the spatial distance changed cross the boundary position. The medians of the two distributions with and without auxin treatment differed by less than 1%. **(D)** The probability for each genomic position to be a single-cell domain boundary in cells without (left) or with (right) auxin treatment.
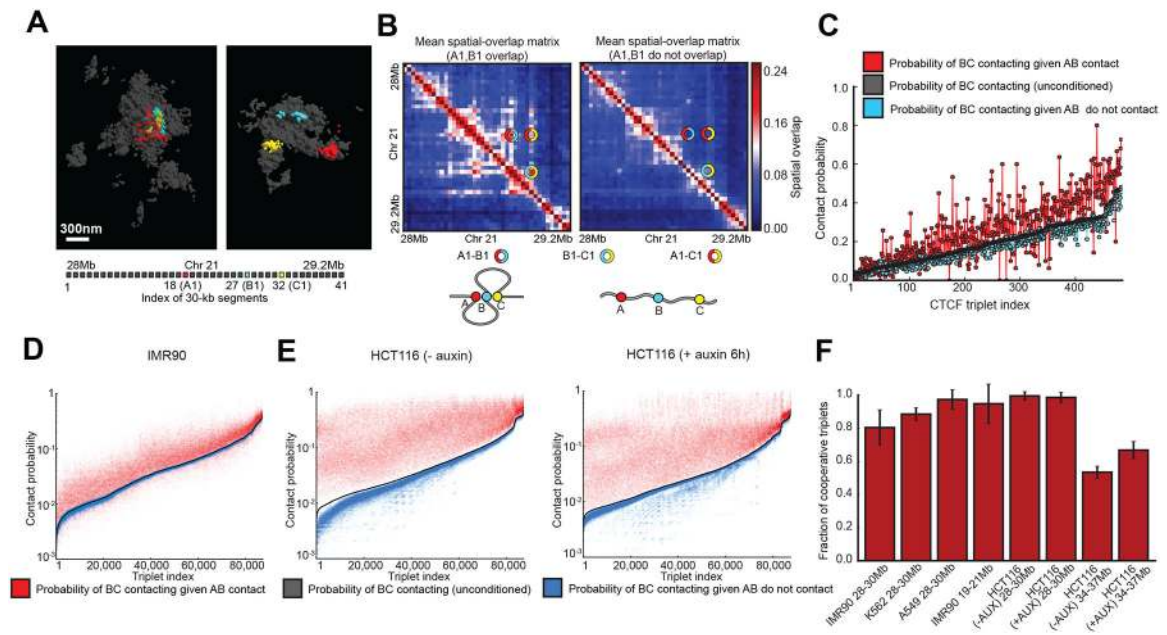
Fig. 5. Cooperative three-way interactions between chromatin segments.
(A) 3D STORM images of a 1.2-Mb region of interest (Chr21:28Mb-29.2Mb) in one of the two copies of Chr21 in two different IMR90 cells. The entire genomic region is represented in gray and three specific 30-kb segments harboring CTCF sites – segments 18 (A1), 27 (B1) and 32 (C1) are highlighted in red, cyan and yellow, respectively. **(B)** Cooperative interactions between a specific triplet of segments A1, B1 and C1. Left: The mean spatial-overlap matrix in the subpopulation of chromosomes where segments A1 and B1 overlap. Right: The mean spatial-overlap matrix in the other subpopulation of chromosomes where segments A1 and B1 do not overlap. Circles indicate the matrix elements corresponding to segment pairs A1–B1 (red-cyan), B1–C1 (cyan-yellow) and A1–C1 (red-yellow). **(C)** Cooperative interactions among all possible CTCF-site triplets in the 1.2-Mb imaged region. Shown in the plot are probabilities with which segments B and C contact in individual IMR90 cells under the condition that segments A and B contact (red) or do not contact (blue) for all ordered combinations of CTCF triplets (~500 total) in the imaged region. "Ordered" means B lies between A and C along the genomic coordinate. Also plotted is the unconditioned probability of B and C contacting regardless of whether A and B contact (black). The index of the triplets is sorted such that the unconditional probability is displayed in ascending order. **(D)** As in (C) but for all ordered triplets of chromatin segments in an extended 2-Mb region of interest (Chr21:28Mb-30Mb) regardless of whether the segment contains CTCF sites. There are ~90,000 such triplets in total, among which only ~2,000 are CTCF-site triplets (i.e. all three segments containing CTCF-binding sites). **(E)** As in (D) but for the HCT116 cells without (left) or with (right) auxin treatment. There are ~90,000 such triplets in total, among which only ~700 are CTCF-site triplets. **(F)** The fraction of triplets of segments that show cooperative interactions (i.e. the triplets for which the probability with which segments B and C contact in individual cells under the condition that segments A and B contact is higher than the unconditioned probability of B and C

contacting regardless of whether A and B contact) for each imaged region in various cell types and cohesin depletion conditions.